Journal of Alloys and Compounds 887 (2021) 161426

Contents lists available at ScienceDirect

Journal of Alloys and Compounds

journal homepage: www.elsevier.com/locate/jalcom

Multiscale microstructural heterogeneity and mechanical property scatter in Inconel 718 produced by directed energy deposition

Yong Chen Yeoh[b], Guido Macchi[d], Ekta Jain[a], Bernard Gaskey[a], Sudharshan Raman[b], Grace Tay[c], Davide Verdi[c], Alin Patran[c], Antonio Mattia Grande[d], Matteo Seita[b,e,*]

[a] School of Mechanical and Aerospace Engineering, Nanyang Technological University, 639798 Singapore
[b] Singapore Centre for 3D Printing, School of Mechanical and Aerospace Engineering, Nanyang Technological University, 639798 Singapore
[c] Advanced Remanufacturing and Technology Centre, A*STAR Research Entities, 3 Cleantech Loop CleanTech Two, 637143 Singapore
[d] Department of Aerospace Science and Technology, Politecnico di Milano, Via Giuseppe La Masa, 34, 20156 Milan, Italy
[e] School of Materials Science and Engineering, Nanyang Technological University, 639798 Singapore

ARTICLE INFO

Article history:
Received 3 May 2021
Received in revised form 20 July 2021
Accepted 31 July 2021
Available online 2 August 2021

Keywords:
DED
Microstructure
Mechanical properties
Solidification
Inconel 718
Hall-Petch

ABSTRACT

Directed energy deposition (DED) is an additive manufacturing technique that enables rapid production and repair of metallic parts with flexible geometry. The complex nature of thermal and material transport during DED can yield unwanted microstructure heterogeneity, which causes scatter in parts performance. Here, we investigate microstructure variations at different length scales in Inconel 718 produced by powder-blown DED using different deposition rates. We quantify spatial trends in grain structure, texture, composition, and solidification structure within parts and correlate them with variations in hardness, yield strength, and Young's Modulus to highlight the effect of the thermal environment during solidification. We find that the high energy input employed when using high deposition rates is conducive to significant microstructure heterogeneity along both the build and transversal directions, which stems from the asymmetric cooling rates generated by the deposition strategy used. We also find that standard heat treatments employed on Inconel 718 are not suitable to homogenize the microstructure. These results have important implications for the development of industrially relevant build rate strategies for additively manufactured parts.

1. Introduction

Metal additive manufacturing (AM) is emerging as an important complement to conventional subtractive techniques, particularly to produce parts with complex geometry. Recently, powder-blown implementations such as directed energy deposition (DED) have been developed alongside more heavily documented powder bed-based methods [1,2]. DED involves a movable high-power heat source (e.g., a laser-beam) that is focused onto a metallic substrate to create a localized melt pool. New material is added to the build in a layer-by-layer fashion by continuously conveying the feedstock material into the melt pool [2]. DED has benefits in production rate, especially for relatively sparse designs with significant void space. It enables modification or repair of existing parts [3], and the combination of different materials within the same build [4].

Significant research effort has been devoted to understanding the particular relationships between AM strategies [5], microstructural characteristics [6,7], and mechanical properties [5,8]. Compared to traditional manufacturing techniques, AM adds an additional layer of complexity to this traditional materials science paradigm due to the dynamic nature of the manufacturing process. As the melt pool moves across the build, complex thermal and diffusion gradients constantly change the solidification conditions [9]. Scanning strategy [10–12] and position within a build [13] can interact to change both local and bulk thermal history, directly influencing microstructural characteristics such as crystallographic texture [9–12], grain size [9,11,14], solidification structures [9,17], and defect density [7,15].

Compared to powder bed-based methods, thermal characteristics of the melt pool are particularly variable in DED due to the lack of a powder bed to conduct heat away from the free surfaces of the build [16–18]. Because heat transfer is mainly dominated by conduction through previously deposited material, variable thermal buildups may occur and cause significantly different, local cooling rates as a part is built. This phenomenon may lead to a multiscale

* Corresponding author at: Singapore Centre for 3D Printing, School of Mechanical and Aerospace Engineering, Nanyang Technological University, 639798 Singapore.

https://doi.org/10.1016/j.jallcom.2021.161426
0925-8388/

microstructure heterogeneity that includes gradients in composition—which stem from differences in solute segregation and diffusion—and in the grain and sub-grain structure—which are function of the deposition strategy employed—even within parts produced using constant DED parameters.

Thermal buildups and microstructure heterogeneity in DED are exacerbated when using a high energy input to enable high deposition rates, which are of interest for industrial processing since they increase throughput. The resulting materials may exhibit large property scatter, which casts uncertainty over part performance and thus hinders the adoption of DED technologies for mass-production of consistent and reliable parts [19,22]. Understanding the intricate relationships between these complex microstructures and materials properties would provide an avenue to improving performance prediction models, or to devising novel alloy designs [20,21].

Here, we map the microstructural heterogeneity in Inconel 718 (I718) samples produced by DED using two different deposition rates. We use electron backscatter diffraction (EBSD) to map the grain structure and orientation distribution within the samples, and energy dispersive spectroscopy (EDS) to assess the composition in dendrite region, which consists of a γ-matrix with nano-size γ′ and γ′′ precipitate [17,18]. We find that high deposition rates yield high, non-uniform thermal buildups, which drive the formation of a complex microstructure heterogeneity that includes "bands" of different crystallographic texture, transitions in grain morphology and size, composition gradients, and different solidification structures. We ascribe this heterogeneity—which is absent in samples produced using a low deposition rate—to local and global differences in cooling rate which stem from the high energy input and tool path strategy used. Using a combination of indentation mapping and compression tests, we link this microstructure heterogeneity to local variations in hardness and bulk mechanical properties, which vary in non-trivial ways across the entire build. Our results highlight the importance of assessing the multiscale microstructure heterogeneity in DED materials when optimizing process parameter and deposition strategy for production.

2. Materials and experimental methods

We prepared two cube samples of 20 mm (L) x 20 mm (W) x 20 mm (H) and one large rectangular sample of 30 mm (L) x 30 mm (W) x 40 mm (H) (Fig. 1b, c, d) using plasma-atomized I718 powder (See Table 1 for chemical composition) with a nominal size distribution of 45–106 µm and standard composition (Advanced Powders & Coatings, Boisbriand, Canada).

Table 1
Chemical Composition of the I718 powder.

Element	Ni	Cr	Mo	Nb	Mn	Al	Ti	Fe
Weight (%)	53	19	3	5	0.5	0.5	0.8	Bal.

Table 2
Process parameter setting.

Process parameter	H sample	L sample
Laser Power (W) /Scanning Speed (mms^{-1})	150	70
Layer Thickness (mm)	1.35	0.75
Powder flow rate ($gmin^{-1}$)	20	6
Laser spot diameter (mm)	3	2

We built the samples directly on a 6 mm thick stainless steel 316 L plate firmly clamped on the CNC rotating table of a Trumpf TruLaser Cell 7040 machine with a three-jet nozzle and a 3 kW rating disk laser. We employed a serpentine scanning pattern with the scan lines parallel to the sample diagonal, which we rotated by 90° each layer to alternate the scanning direction (Fig. 1a). The produced cubic samples have identical geometry (Figs. 1b, 1c), but differed in volumetric deposition rate by varying laser power, scan speed, and powder mass flowrate. We used industrial proprietary parameters that were already optimized for full-density builds (see Table 2 for approximate values), which led to "high" (H) and "low" (L) deposition rates of 11.4 mm^3s^{-1} and 3.3 mm^3s^{-1}. Since the deposition rate is a complex function of the different DED parameters [17], we analyze our results based on the input energy density, E. We estimated the corresponding values for sample H and L to be 50 J mm^{-2} and 35 J mm^{-2}, respectively, using:

$$E = \frac{Laser\ \ power}{Scanning\ \ speed\ \ x\ \ Laser\ \ spot\ \ diameter}$$

We produced the rectangular (R) sample using the same process parameters employed for the H sample. We used argon as both carrier gas and shielding gas during sample production.

We relied on an external service provider (Doxon Engineering Pte. Ltd., Singapore) to heat-treat all samples following the method described by AMS 5663 [23], which consists of a solution treatment at 954 °C for 1 h, followed by two age hardening steps at 718 °C for 8 h and 621 °C for an additional 8 h. After heat treatment, we cut the H and L samples into multiple slices along the cross-sectional X-Z plane by means of wire electrical discharge machining (EDM) for microstructure analysis. Conversely, we cut the R sample into 18 compression cylinders of 4 mm diameter and 6 mm height via EDM from the sample centerline, as shown schematically in Fig. 4a. We

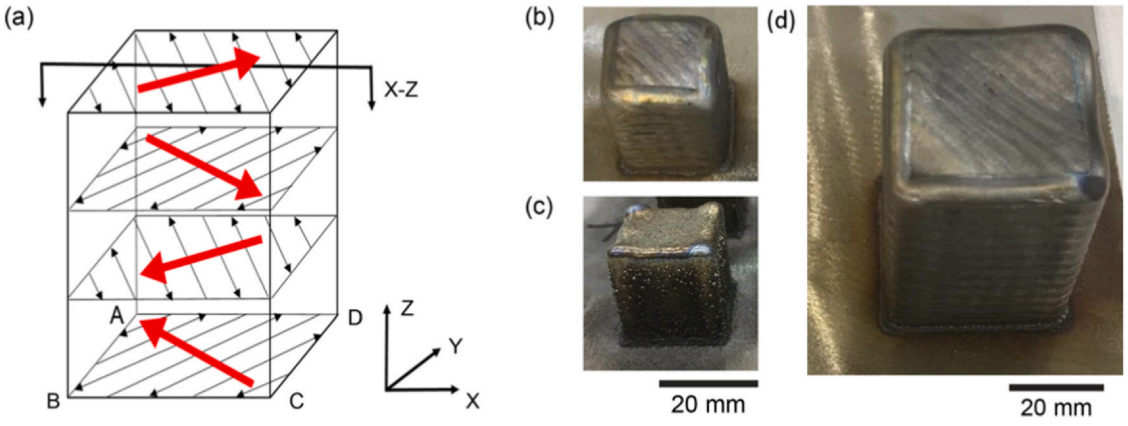

Fig. 1. Sample production. (a) Schematic illustrating the deposition strategy adopted here (black arrows), the resulting thermal gradients (red arrows), and the cross-sectional plane (X-Z) used to analyze samples microstructure. Photographs of I718 (b) H, (c) L samples 20 mm (L) x 20 mm (W) x 20 mm (H) and (d) R sample 30 mm (L) x 30 mm (W) x 40 mm (H) deposited on a stainless steel 316 L substrate.

ground the H and L sample slices to a smooth surface and polished them with 3 µm diamond solution and a 0.25 µm colloidal silica suspension. To reveal the microstructure for metallographic analysis, we etched the polished samples for 7–9 min in a bath of waterless Kalling's solution (5 g $CuCl_2$, 100 milliliters HCl, 100 milliliters Ethanol) [24]. We employed the same surface preparations on the upper circular surface of each cylinder from the R sample. We characterized the samples microstructure using a Nordlys 2 S EBSD detector (Oxford Instruments, UK) mounted to a Jeol JSM 7600 F field emission scanning electron microscope (FE-SEM). We took EBSD measurements using an accelerating voltage of 20 kV, probe current of 20 nA, and step size of 10 µm. We used the same FE-SEM for metallographic investigations to assess the solidification structure, and for compositional analysis of the sample surface by means of EDS. Because we calibrated the EDS measurements prior to every measurement, composition variations across different samples may be directly compared.

We measured hardness across the polished surface of the H and L sample slices using a Nano Indenter G200 (Agilent Technologies) with standard XP indentation head in compliance with the ISO 14577 standard [25]. During nanoindentation, we set the depth limit to 1000 nm, the strain rate to 0.05 s^{-1}, the harmonic displacement to 2 nm, the frequency to 45 Hz, and the Poisson ratio to 0.29 [26]. To calculate the hardness, we defined the lower and upper depth limits at 850 nm and 950 nm, respectively, where the hardness and modulus have approached their asymptotic values. We performed three arrays of 8 × 10 indentations along the centerline of the sample, approximately one quarter, half, and three quarters of the way from the base plate to the top of the build. The spacing between indents within each set was 0.5 mm along X (across the sample surface) and 0.3 mm along Z (in the build direction).

We used a Micro Measurements FM-300e to perform microhardness measurements with a load of 300 g and a dwell time of 10 s. We performed an array of 8 × 25 indentations (along Z and X, respectively) on both samples H and L, and one of 12 × 6 (along Z and X, respectively) on sample R. In samples H and L, we carried out each indentation at an equal distance of 2 mm along Z and 0.15 mm along X. In sample R, we used variable spacing (between 2 mm and 5 mm) along Z and 0.15 mm along X. All measurements were taken along the sample centreline.

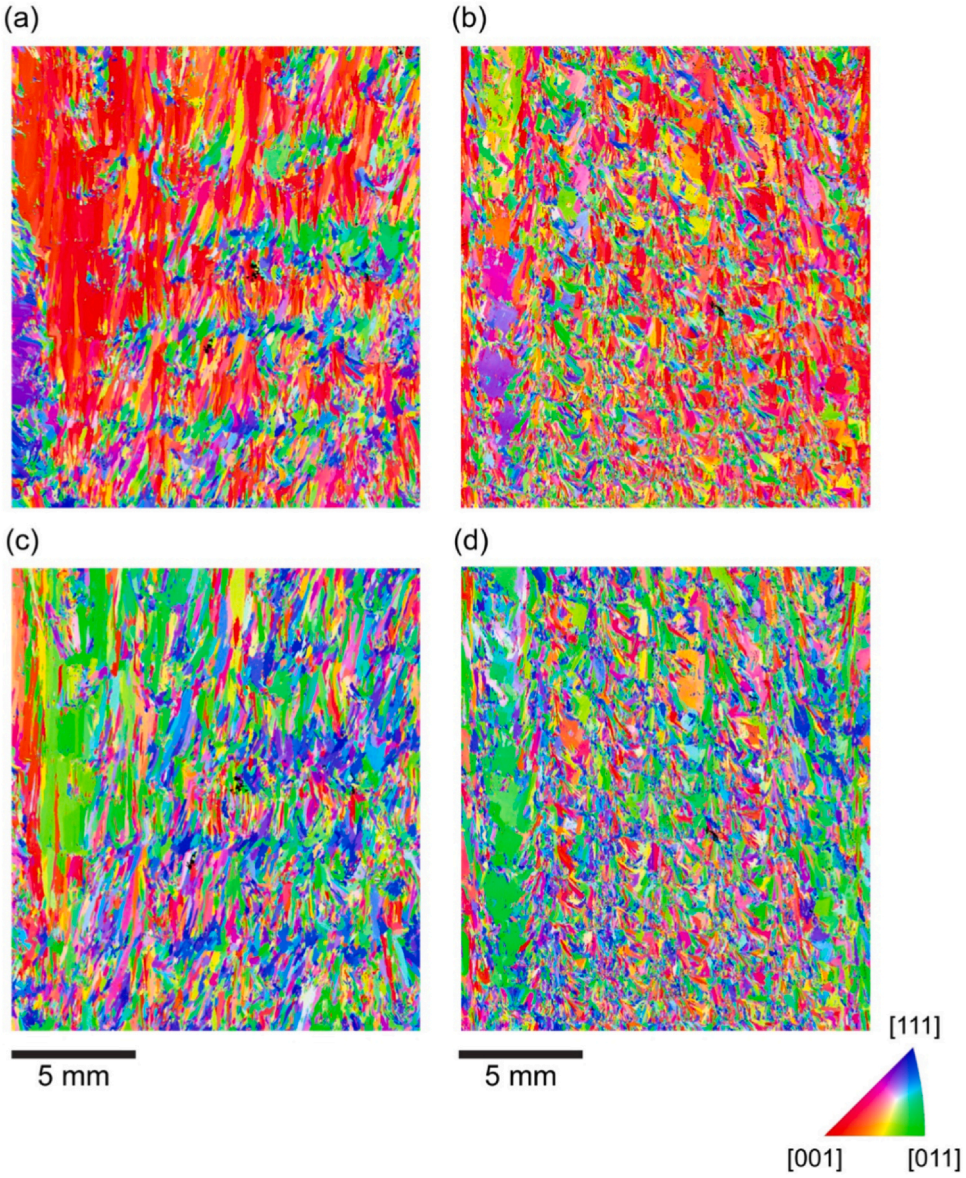

Fig. 2. Grain structure. EBSD grain orientation map along Z (the build direction) for (a) the H sample and (b) the L sample. EBSD grain orientation map along Y for (c) the H sample and (d) the L sample.

We tested all cylindrical specimens in compression, using a displacement-controlled Shimadzu AGS-X 50 kN. Prior to testing, we lathed the pillars to obtain symmetrically flat surfaces. We adopted a strain rate of 0.003 mm/s and assumed quasi-static mechanical testing. During each test, we lubricated the specimens' surface to reduce barreling of the material under compression. Due to the small dimensions of the cylinders, we could not use extensometers and we recovered the actual strain after operating machine compliance. We then performed four loading-unloading cycles in the plastic regime for each cylinder to obtain the elastic properties of specimen.

3. Results

3.1. Grain Structure and Texture Heterogeneity

Fig. 2a, b, c, and d compare the H and L sample microstructures as measured by EBSD. These maps—which show grain orientation along Z and Y—evince a non-uniform grain size and orientation distribution in the H sample compared to the more homogeneous grain structure and texture of the L sample. The H sample exhibits progressively coarser grains with stronger < 100 > texture along Z (Fig. 2a). We also note the presence of "bands" of equiaxed grains interrupting the prevailing columnar, < 100 > -oriented grains with a periodicity that reflects the layer-by-layer deposition process due to the scanning strategy in use. These qualitative trends are confirmed by our quantitative texture and grain size analysis in both samples H and L along Z (Figs. 3 and 4).

To assess texture variations, we divide the EBSD data set from both samples into 0.3 mm thick bins along Z. We select this bin size because it is smaller than the layer thickness in both samples H and L (equal to 1.35 mm and 0.75 mm, respectively). In this way, we avoid averaging texture information across different layers and can study the occurrence of local differences in cooling rate as a function of the deposition strategy used. We compute texture strength in each bin by taking the highest Multiple of Uniform Density (M.U.D.) value in Z direction for grain orientation along the < 100 >, < 110 >, and < 111 > direction. The higher the M.U.D. value, the higher the spatial concentration of a specific grain orientation. The analysis shows that the < 100 > texture strength doubles from bottom to top of the H sample (Fig. 3a), while it does not vary significantly in the L sample (Fig. 3b). Fig. 3a also clearly highlights the texture "banding" which we observe in Fig. 2a. Interestingly, there seems to be an anticorrelation between the < 100 > and the < 110 > texture. In other words, the microstructure "bands" of smaller grains are characterized by a relatively strong < 110 > texture.

To assess grain size variations along Z in all samples, we compute the equivalent circle diameter (ECD) of grains and plot the values in Fig. 4. We notice grain coarsening in samples R (from ~94 µm at the bottom to ~116 µm at the top of the build) and H (from ~100 µm at the bottom to ~115 µm at the top of the build), but no significant difference in sample L (from ~60 µm at the bottom to ~65 µm at the top of the build). The analysis also shows that the average grain size in samples H and R is comparable and ~60% larger than that in sample L. Indeed, when comparing the grain coarsening trends in samples H and R over same length (i.e., up to 20 mm), we compute the same increase of 15% in the two samples. This result is expected since we used the same process parameters to produce both H and R samples, which led to higher deposition rates—and thus higher energy input—compared to the L sample. Hence, H and R samples experienced similar thermal history during processing. Moreover, we notice that grain size variations in sample H reflect the presence of the microstructure "bands" seen in Figs. 2a and 3a, confirming the smaller average grain size in those regions. The "banding" is not visible in Fig. 4c because of the sparse data points we collected from upper circular surface of cylinder extracted from sample R (Fig. 5a).

The corresponding EBSD data set for this sample is shown in Fig. 5. Here, we acquired EBSD scans from the top surface of each individual compression cylinder, taken from different locations across the R sample (Fig. 5a). Qualitatively, the grain structure in these maps matches the trends shown in Fig. 4c. We also find a consistently smaller average grain size along X—with the right-hand side of the sample in the cross-section exhibiting the smallest value—and a change in texture from < 100 > (on the left-hand side of the sample) to random (at approximately X = 20 mm).

Overall, our texture and grain size results are consistent with the findings on DED I718 by Parimi et al. [33], who reported complex microstructures consisting of regions of fine, randomly oriented grains in the lower part of the build—closer to the cold

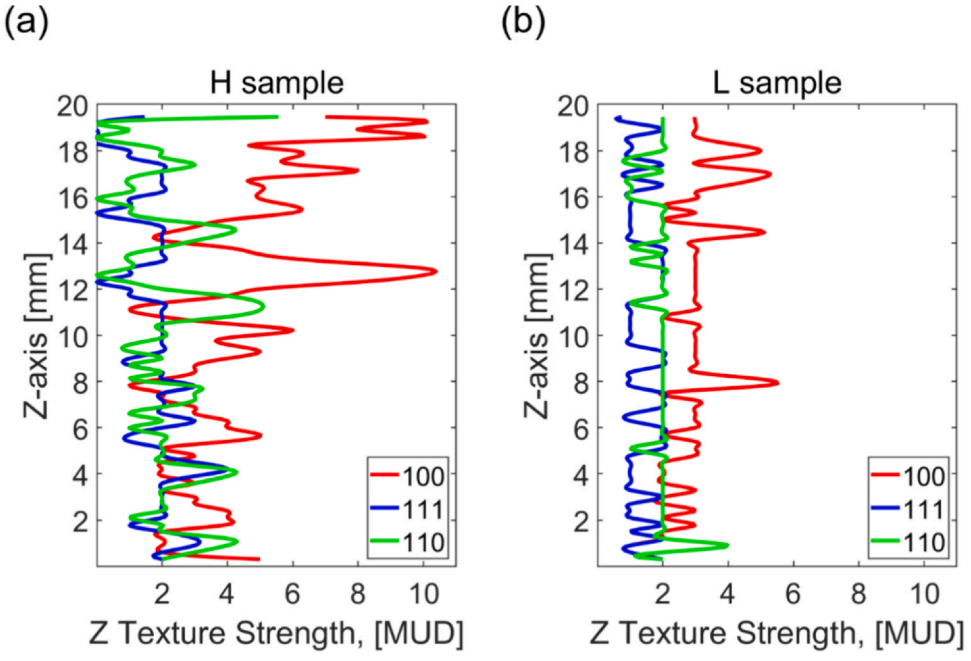

Fig. 3. Texture analysis. Texture strength density plot along Z-axis for (a) H sample and (b) L sample.

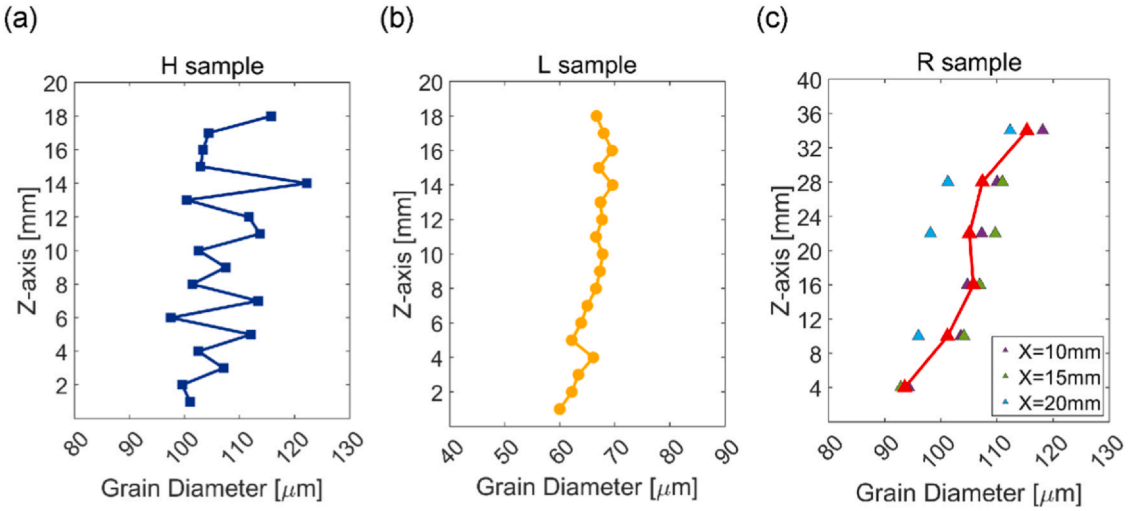

Fig. 4. Grain structure. (a) Grain diameter of H sample along Z (b) Grain diameter of L sample along Z (c) Grain diameter of R sample along Z at different X location.

substrate—and regions of coarse, columnar grains with strong < 100 > texture parallel to Z in the higher part of the build. The alignment of grain growing axis with the < 100 > direction is often found in directionally solidified FCC alloys, and controlled by the anisotropic crystal growth rate [41].

3.2. Compositional heterogeneity

Besides the differences in grain structure and texture, we also investigate variations in the spatial distribution of the inter-dendritic phases and precipitates that are commonly found in I718. The as-printed inter-dendritic structure is dominated by a Nb-rich phase referred to as Laves phase, which forms upon coalescence of γ-matrix dendrites during solidification of the melt pool. Upon heat treatment, the Laves phase decomposes and a fraction of Nb diffuses into the dendrites to form γ'' precipitates [17]. The Nb fraction that remains in-between dendrites leads to the formation of small clusters of aligned platelets of δ-Ni_3Nb, which is another well-known strengthening precipitate [27]. This phase inherits improved corrosion resistance brought about by Nb, which makes it more resistant to chemical attack compared to the γ-matrix. For this reason, δ platelets are readily visible protruding from the inter-dendritic area across the sample surface after chemical etching (as shown in Fig. 6). Using this preparation technique, we qualitatively observe the precipitate geometry and distribution in sample H and L by scanning electron microscopy (SEM). We find a progressive increase in density and size of δ platelets along Z on the H sample. δ platelets are hardly observed at the bottom of the build but clearly visible at the top of the build, as shown in Fig. 6a–c. Conversely, the L sample shows a uniform distribution of δ platelets along Z (Fig. 6d–f). To investigate the origin of this change in precipitate structure in the H sample, we take EDS line-scan measurements along individual dendrites (see inset in Fig. 6g) to assess the composition of the matrix (i.e., the regions within dendrites) across the sample height in both samples. We take a series of such measurements uniformly spaced in X and Z every 4 mm and 2 mm, respectively. From these measurements, we compute the average Nb concentration in the γ-matrix along X and plot it versus Z (Fig. 6g). We note that the Nb concentration follows different trends in the two samples. We correlate these trends with spatial variations in the density and size of δ platelets and use them to estimate the amount of Nb in solid solution as well as that which leads to the formation of γ'' precipitates in the γ-matrix, which are not resolvable by means of SEM [18]. Because the mean Nb content—which includes the Nb contained in δ platelets, as well as that within the dendrites—is constant throughout the builds and equals the nominal concentration in I718 (Table 1), the fraction of inter-

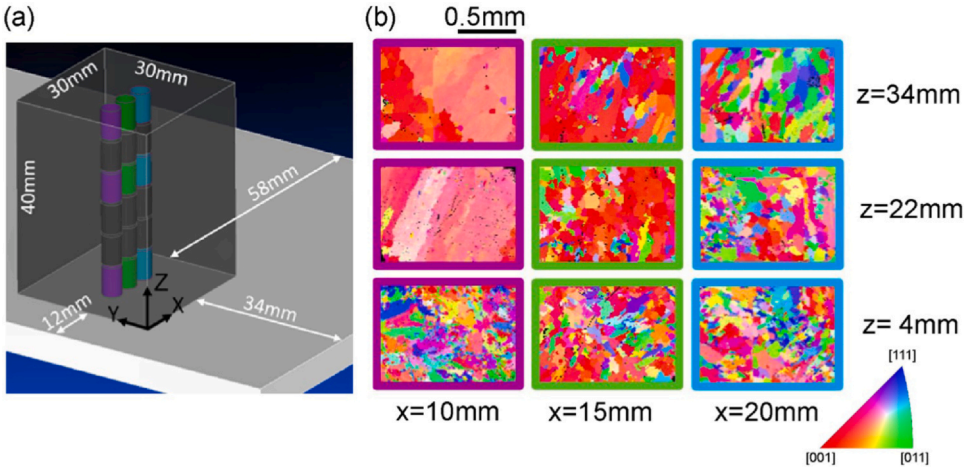

Fig. 5. Grain structure. (a) CAD draw showing compression cylinders distribution in R sample (b) EBSD grain orientation map along Z for the upper circular surface (parallel to the XY plane) of the compression cylinders.

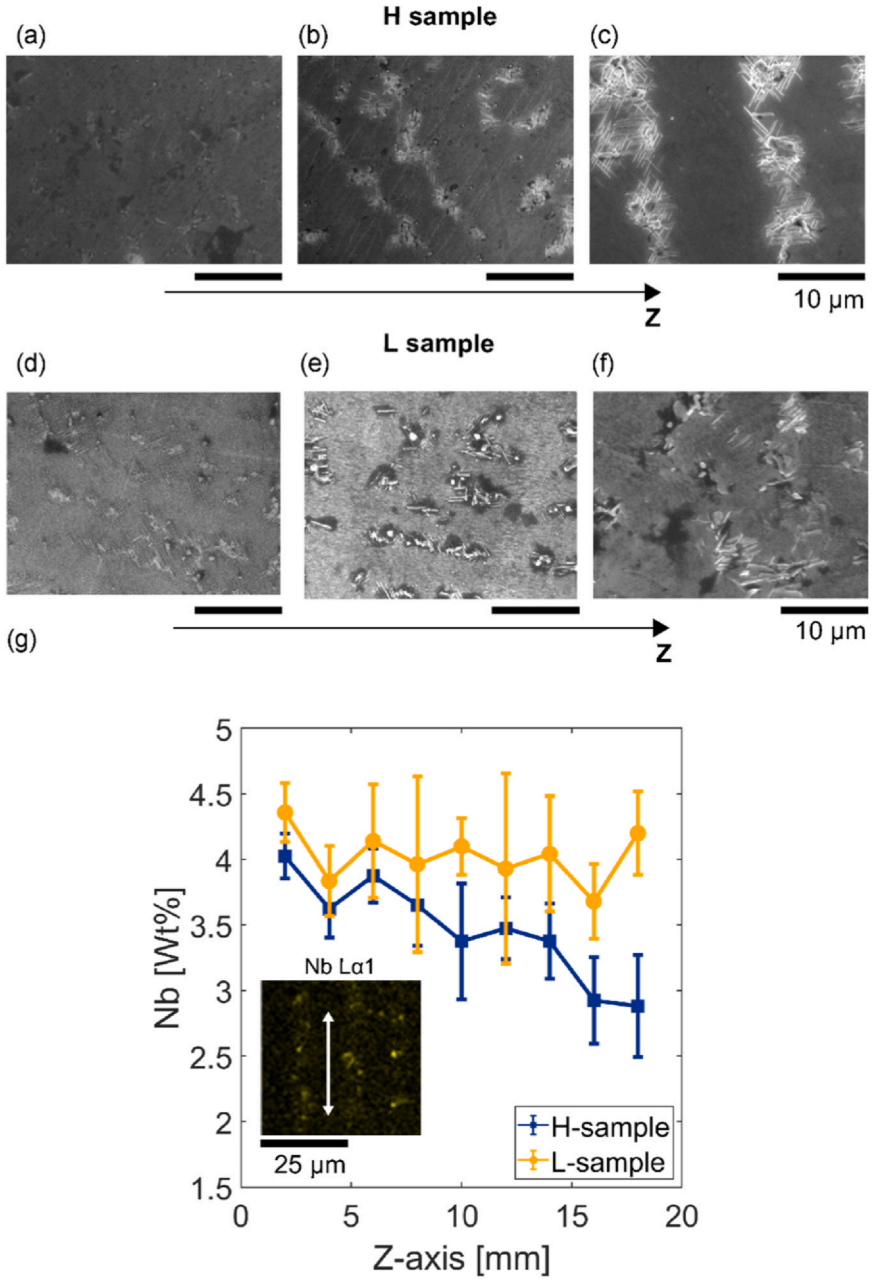

Fig. 6. Precipitate distribution. Secondary electron micrographs showing the local H (a, b, c) and L (d, e, f) sample surface along Z, from (a, d) bottom of the build (approximately 2 mm from the base plate), (b, e) the approximate middle, and (c, f) the top (approximately 16 mm from the base plate). The micrographs illustrate qualitatively the change in δ platelet density in H sample. (g) Nb content change along Z as measured along dendrites (as indicated by the white arrow in the inset map) by EDS in both the H (dark blue) and L (light blue) sample. The inset shows a representative EDS Nb map on the H sample surface approximately 16 mm from the base plate. Nb is mainly concentrated in the inter-dendritic regions.

dendritic δ phase must be inversely proportional to the Nb concentration within dendrites and, in turn, to the fraction of nano-sized precipitates that form during the aging treatment [17,18]. In other words, regions in which we measure higher (respectively lower) Nb by EDS exhibit sparser (respectively denser) distribution of smaller (respectively larger) δ platelets (Fig. 6a–c). In the H sample, we measure more than 4 wt% of retained Nb in the dendritic regions near the bottom of the build and less than 3 wt% at the top of the build, as shown in Fig. 6g. By contrast, the L sample exhibits a more consistent mean Nb concentration along Z, but larger deviation. We attribute the latter to the finer feature size in the L sample, which makes it harder to avoid the Nb-rich δ platelets during EDS line scan.

3.3. Cooling rate variation during DED

We attribute the compositional gradient and microstructure differences in samples H and L to changes in cooling rate (CR) brought about by different energy input used. The high energy input in sample H amplifies the thermal buildup along Z and drives higher Nb segregation in the inter-dendritic region as the build progresses. Since we produced samples H and R using the same process parameters, we expect the latter to exhibit similar trends in CR, microstructure (as confirmed in Fig. 5b), and composition. However, the sparse data set and large size of the R sample prevented us from carrying out a detailed CR analysis as we did for the sample H.

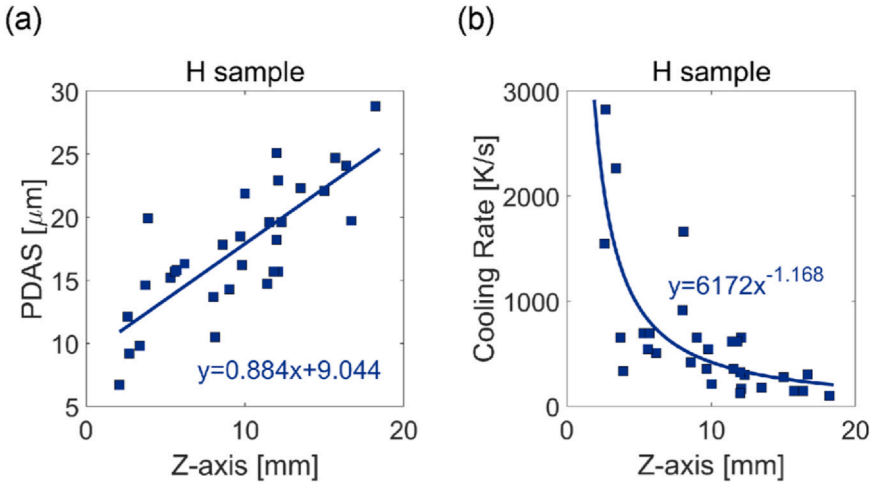

Fig. 7. Solidification kinetics. (a) Variation of PDAS along Z in the H-sample. (b) Corresponding CR computed using Eq. (1).

To evaluate the relative changes in CR quantitatively in the H sample, we measure the primary dendrite arm spacing (PDAS) by means of SEM. We perform a total of 34 sets of PDAS measurements on different grains with similar orientation. Specifically, we select grains with < 100 > orientation along Z and < 110 > along Y, such that the PDAS can be measured directly without correcting for perspective error. Fig. 7a shows that PDAS increases along Z, indicating a progressive decrease in CR as more material is deposited. To quantify the CR from PDAS, we use the empirical relationship [28–30]:

$$PDAS = K(CR)^{-n} \quad (1)$$

where K and n are material dependent constants, which reported to be 130 and 0.33, respectively [31]. The resulting change in CR along Z in the H sample is plotted in Fig. 7b. We compute a difference in CR from ~2800 K/s at the start of the build to ~100 K/s at the end of it. This result corroborates the hypothesis that the local thermal environment changes more abruptly at the beginning of the build because of the high heat extraction rate of the substrate and the high energy input employed during high deposition rate DED builds. Assessing PDAS in grains with similar orientation and computing CR for the L sample is difficult because of the finer grains as compared to the H sample. However, random measurements across the surface of sample L suggest that PDAS is more consistent across the build and of the order of 5 µm. These differences in CR within and across the samples correlate well with the spatial heterogeneity in microstructure and composition reported in Figs. 2, 3, 4 and 6.

3.4. Mechanical Heterogeneity

To quantify the effects of the measured microstructural and compositional heterogeneity on the alloy mechanical properties, we probe variations in the local hardness on all 3 samples along Z using micro- and nanoindentation (Fig. 8). In the H sample, both types of measurements indicate that hardness is highest near the start of the build—close to the base plate—but decreases progressively moving away from it. Conversely, the dispersion of the measured hardness increases along Z (Fig. 8a). The relative change in local hardness of the H sample is striking when comparing histograms of nanoindentations taken near the base plate with those near the top of the sample (Fig. 8d). The average hardness varies by 5% and 9% in micro- and nanoindentation measurements, respectively. In both measurements, the standard deviation of the dataset more than doubles from bottom to top, indicating a general increase in the dispersion of the local hardness. We observe the exact same trends when probing the micro-hardness in the R sample (Fig. 8c), with the stark difference that the hardness value plateaus towards the top region of the build. This plateau suggests the establishment of a CR steady-state. From the bottom of the sample to when the hardness value reaches a plateau (at around Z = 20 mm), we measure an average micro-hardness variation of ~8%.

As expected, the more uniform microstructure and composition in the L sample yields no significant variation in hardness (Fig. 8b). The measured hardness values lie within the same margin of error throughout the whole build. Moreover, the dispersion of individual measurements is also relatively constant. The smaller variation between measurements in this sample suggests more consistent hardness along Z. This greater uniformity has implications on the macroscopic mechanical performance of the entire part.

Grain size and crystallographic texture are known to affect the yield strength and elastic/plastic anisotropy of metal alloys [42–44]. To investigate how large-scale variations in texture and grain size affect the bulk mechanical properties in DED I718 we plot and analyze the engineering yielding point and elastic modulus of the R sample along Z and X (Fig. 9a and b, respectively). Owing to its large size, the R sample is ideal to perform series of compression tests and assess these properties at a larger scale compared to what is achievable by indentation tests. We find both strength and modulus of elasticity to decrease along Z, but to increase along the X-axis. In contrast to hardness, we record no appreciable plateau in either property along Z. The decrease in strength along Z matches the grain size variation seen in Fig. 4b according to the well-known Hall-Petch relationship (discussed in detail in the following section) [38]. At the bottom of the build, we observe no difference in strength along X, which reaches a value of ~980 MPa (the highest measured in our experiments). In this region, the high CR resulting from the large heat sink effect associated with the base plate drives the formation of fine grains of similar size (Fig. 4c) with high concentration of Nb in the γ-matrix (assuming the measurements in Fig. 6 can be extended to sample R). However, differences in yield strength along X become more prominent as the distance increases from the base plate (Fig. 9a). In general, we find the yield strength value at the right-hand side of the sample cross-section (X = 20 mm) the highest. This result is in line with the average grain size measurements at different X-coordinates along Z (Fig. 4c).

We attribute the decrease in Young's modulus along Z and X (Fig. 9b)—which we compute from the unloading of compression cylinders—to the variation of texture across the sample. Along Z, we observe 19%, 15%, and 4% decrease in Young's modulus for X = 10 mm, X = 15 mm, and X = 20 mm, respectively (Fig. 9b). The large difference in Young's modulus found at X = 10 mm (i.e., the left-hand side of the

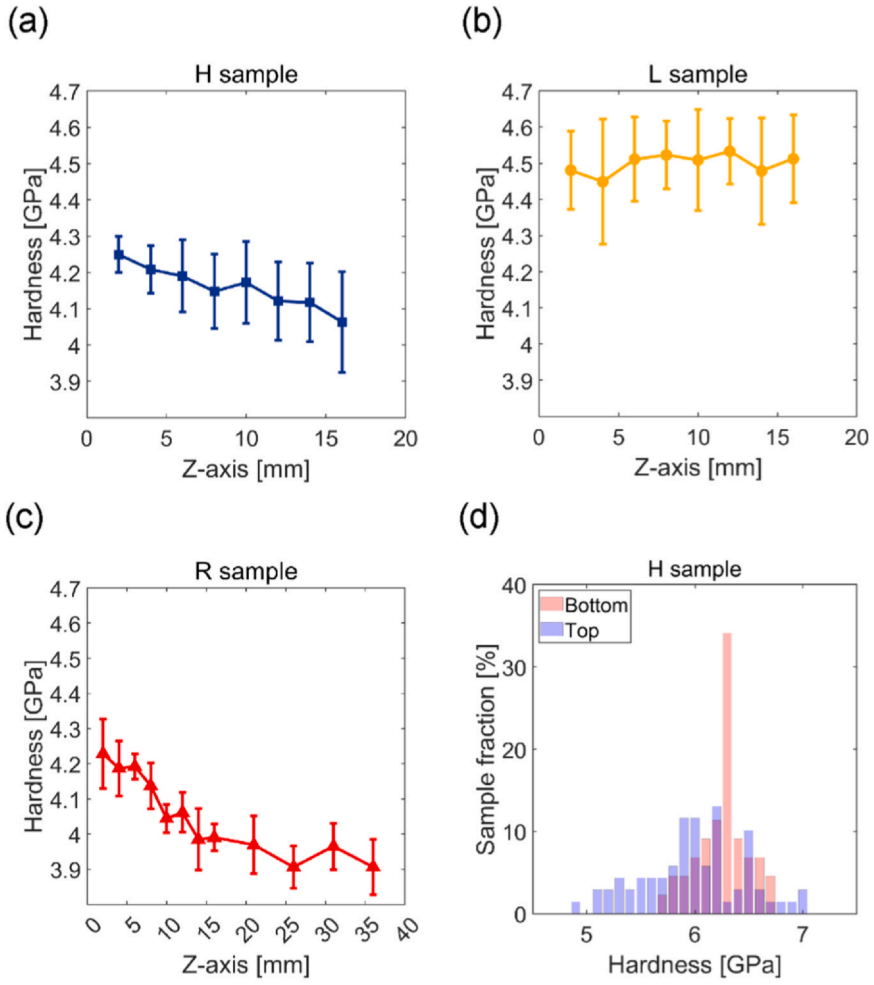

Fig. 8. Mechanical heterogeneity. (a) Plot of microhardness in the H sample, (b) Plot of microhardness as a function of distance from the base plate. (c) Microhardness of the R sample across 40 mm from the start of the build. (d) Nanoindentation hardness histograms from the bottom (red) and the top (blue) of the same sample.

R sample cross-section) is probably due to the combined effect of the texture transition from random to < 100 > and the grain structure transition from equiaxed to columnar (Fig. 5b). Along X, the Young's modulus computed from measurements at X = 20 mm is the highest and most consistent. We attribute this to the random grain orientation and equiaxed grain structure in this region of the R sample.

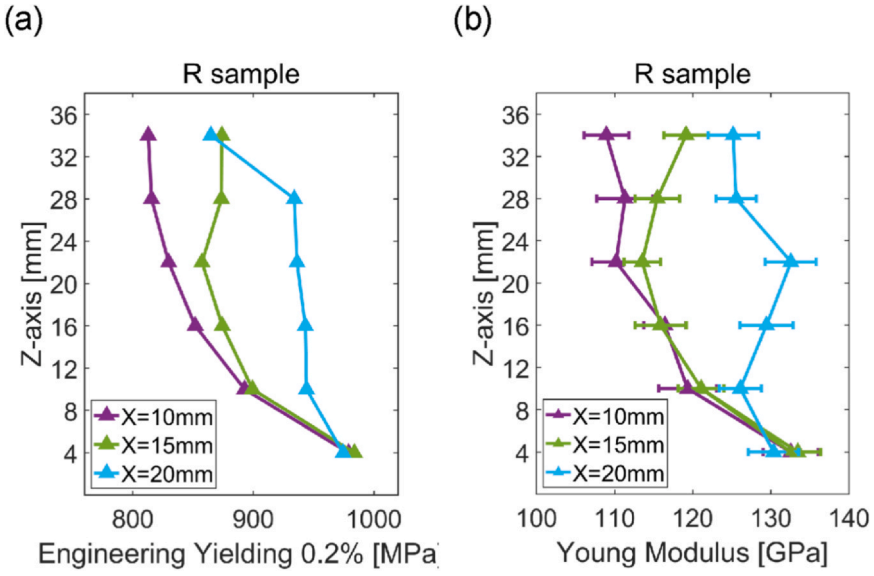

Fig. 9. Elastic and mechanical properties distribution. (a) Engineering yielding of the compressed pillars along the build direction Z (b) Young modulus along Z, averaged from the four loading unloading cycles within each stress strain curve.

4. Discussion

4.1. Heterogeneity along the building direction

In DED processes, parts naturally heat up during production. Conduction to the substrate contributes a significant fraction of the total heat removal, and the path to the substrate grows together with the build while the heat input remains constant [1]. When I718 is deposited at higher deposition rates using high energy density, parts can be glowing red or orange upon completion, roughly corresponding to temperatures exceeding 700 °C. This temperature increase has direct effects on the microstructure. First, it acts as a cyclic heat-treatment on the early parts of the build, coarsening their microstructure as subsequent material is added, which is clearly observed in both H and R sample produced with same deposition strategy. A second consequence is the change in thermal environment around the melt pool, which affects the CR. As the solid region around the melt heats up, the CR diminishes resulting in the formation of larger grains with stronger crystallographic texture [31,32]. Conversely, the more fine-grained areas are associated with regions of high CR. These regions are more prevalent towards the lower part of the build—which is closer to the cold substrate—or in certain layers, where the area had the longest time to cool down.

These phenomena can be readily observed in the H and R sample, which exhibits progressively stronger < 100 > texture and coarser grains along Z (Fig. 2a). Our microstructure analysis of the H sample (Figs. 3a and 4a) confirms a higher density of < 100 > textured grains with larger equivalent circular size near the top. A similar trend is observed in R sample too (Figs. 4c and 5b). The higher heat accumulation rate towards the top of the build—which leads to lower CR—promotes re-melting of the previous layers, which in turn leads to epitaxial growth of columnar grains with their fastest growth direction parallel to Z. These effects become more pronounced in large-scale parts. Indeed, we measure ~15% increase in average grain size in sample H (which is 20 mm tall), but a remarkable 23% in sample R (which is 40 mm tall). Conversely, the L sample exhibits smaller and more consistent grain size along Z, indicating lower heat accumulation and hence uniform cooling rate.

Beside the microstructure coarsening and strengthening of the < 100 > texture along Z, the high energy input employed while using high deposition rate in DED I718 also leads to peculiar microstructure "bands" consisting of fine grains with different texture (in this case < 110 >), which interrupt the columnar growth with a periodicity of about two layers. In our sample, we attribute the origin of the "bands" to serpentine scanning strategy used during DED. With reference to Fig. 1a, and calling A, B, C, and D the four corners of each layer, when a first layer is deposited the serpentine raster starts at point A and ends at point C. Upon completion of the layer, this raster strategy leads to the establishment of a transverse thermal gradient, with point A (the colder) having cooled for longer than point C (the hotter). When the second layer is deposited the serpentine raster rotates by 90° and moves from point B to point D. In this second layer, points A and C lie along the same scan line and thus are printed almost simultaneously, halfway through the layer onto areas with different temperatures (i.e., points A and C in the first layer). Conversely, B and D are the first and last point printed in the second layer, but they were printed nearly simultaneously in the first layer. In this example, point A will have cooled for one and a half layers of printing time while point B will be heated up again after only half a layer of printing time. That results in a factor 3 difference in cooling time within a single layer. As additional layers are added, each corner will have two long cooling times followed by two much shorter cooling times, which would result in possible microstructure heterogeneity with a repeat unit of two build layers. However, the thickness and extent of the finer, randomly textured "bands" decreases as the sample grows because of the prevailing thermal buildup along Z. Similar "banded microstructures" were observed by Parimi et al. [33] in DED I718 thin walls and were attributed to the inter-layer idle time difference when using unidirectional and bi-directional scanning strategies. In our samples, the "banded" grain structure and texture are the result of sample geometry (a cube rather than a thin wall) and the high laser power employed, which enhances differences in thermal buildups across different layers even though the scanning strategy is kept constant throughout the build. Because of the lower energy input and thus lower thermal buildup, we observe no "banding" in the L sample. The "banding" in sample H is not to be confused with that which arises from compositional or phase changes found in the heat affected zone in DED samples [51]. The optical micrograph in Fig. S1 shows the individual melt pool boundaries across sample H. This micrograph indicates no presence of "bands" that could be attributed to the heat affected zone. Moreover, if the "bands" we find in this sample were associated with the heat affected zone, they should appear at the interface between each deposited layer and not with a periodicity of two layers.

The fact that the "bands" exhibit a < 110 > texture is also an interesting observation. A possible reason for this texture transition may be that these regions have cooled down for longer compared to the inter-band regions of the sample. As a result, the local thermal gradients within the melt pool may be more sensitive to the melt pool geometry than to the prevailing heat flux along Z. Several researchers have shown that in these cases the local thermal gradients may grow at an angle with respect to the build direction and lead to the establishment of a < 110 > texture along Z [45,46]. The reason why these bands appear to have a more equiaxed grain structure compared to the < 100 > -textured regions could also be attributed to the growth direction of these grains. Following the tilted thermal gradients, grains in these "bands" may grow out of the sample (X-Z) plane and thus be imaged along their cross-section.

The change in CR along Z described in Fig. 7 contributes not only to large-scale changes in grain structure and crystallographic texture; it also affects the local elemental distribution in the alloy and the solidification structure (i.e., the size of the dendrites). A lower CR gives rise to coarser dendrites (and larger PDAS values) and promotes partitioning of alloying elements at inter-dendritic regions (as seen in the inset in Fig. 6g), decreasing solute content in the intra-dendritic regions [34]. This latter effect should be most pronounced in high melting point alloying elements such as Nb (melting point 2477 °C), which have the greatest partition coefficient at the solid-liquid interface [35]. Although the overall composition of I718 is consistent throughout the part (as confirmed by EDS analysis), the local Nb content in the dendritic region varies measurably along Z in the H sample (Fig. 6g). We also measure the concentration of other solute elements (such as molybdenum, aluminum, and titanium) along Z using EDS, but find no significant variation (see Fig. S2).

To investigate the combined effect of this multiscale microstructure heterogeneity on the alloy mechanical properties along the build direction, we plot hardness versus grain size, texture, Nb content, and PDAS in the H sample in Fig. 10a–d, respectively. These plots indicate no direct correlation between variations in grain size and texture (taken along the direction parallel to the loading axis) with hardness. By contrast, we find strong correlation between the hardness trend and variations in Nb concentration and PDAS. To estimate the relative contribution of these microstructural features on the alloy strength, we consider the strengthening mechanisms associated with the grain boundary fraction (σ_{GB}), solute concentration in solid solution (σ_{SS}), precipitates ($\sigma_{\gamma'}$ & $\sigma_{\gamma''}$), and dendrite spacing (σ_{PDAS}). To this end, we use the yield strength model established by Shuya Zhang [49] and infer hardness across our sample. We provide details about the model and the calculations of

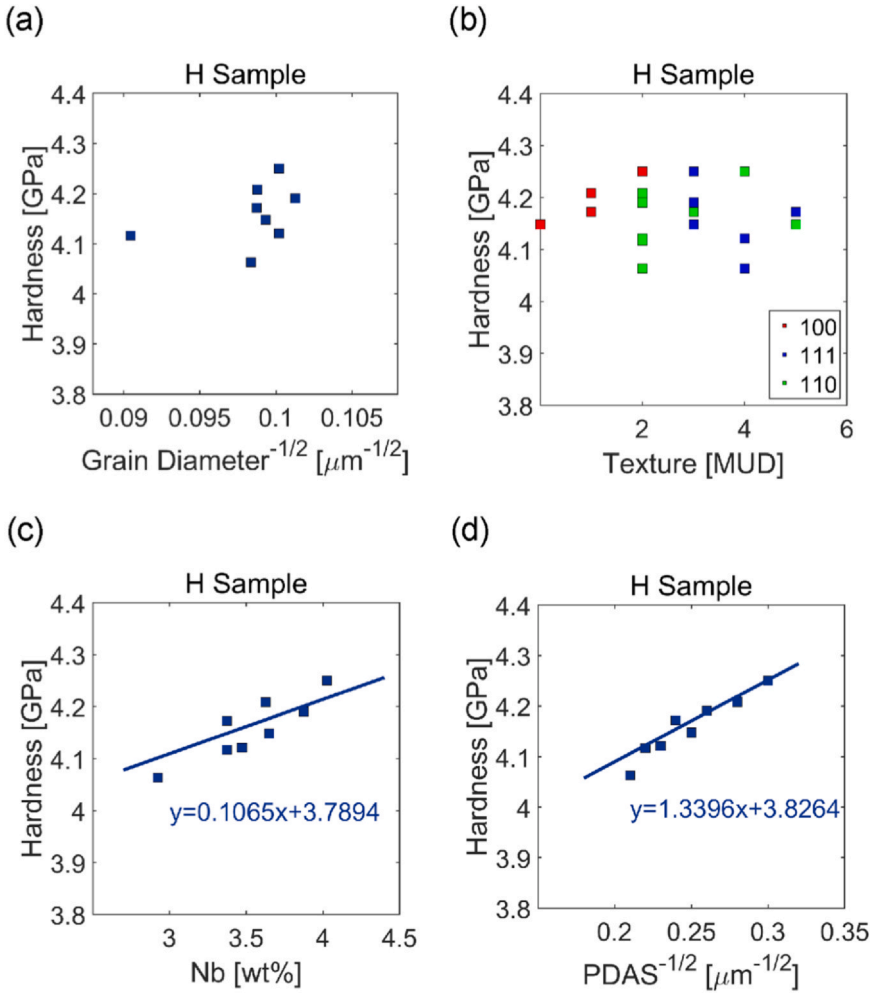

Fig. 10. Effect of solute distribution. (a) The relationship between micro hardness and grain diameter (b) The relationship between micro hardness and texture (c) The relationship between micro hardness and local Nb wt% in the γ-matrix. (d) The relationship between micro hardness and PDAS.

Table 3
Hardness contribution in sample H, considering the intrinsic strength, σ_0, grain boundary strengthening, σ_{GB}, solid solution strengthening, σ_{SS}, dendrite spacing strengthening, σ_{DAS}, γ''strengthening, $\sigma_{\gamma''}$, and γ'strengthening, $\sigma_{\gamma'}$. We provide the detailed calculations for each strengthening mechanism in the Supplementary Information.

Hardness		Δ Hardness$_{Top-Bottom}$	
H sample	Contribution	Δ GPa	Contribution
σ_0	5%	0.00	0%
σ_{GB}	8%	0.02	11%
σ_{SS}	31%	0.03	15%
σ_{PDAS}	1%	0.04	22%
$\sigma_{\gamma''}$	41%	0.11	53%
$\sigma_{\gamma'}$	15%	0.00	0%
$\sigma_{hardness}$	100%	0.20	100%

all contributing factors to the alloy strength in the Supplementary Information. We report the main results in Table 3. Among the different microstructural features, we find the precipitate content and Nb concentration in solid solution to contribute the most to the variations in hardness along Z. While a progressively larger grain size is conducive to a decrease in hardness (following the Hall-Petch relationship), our calculations predict that grain size variations accounts for only 11% difference in hardness from bottom to top of sample H. This result confirms the lack of correlation seen in Fig. 10a. Moreover, we estimate the contribution stemming from the increasing size of dendrites to account for 22% of the hardness variation. It is well known that the solidification structure—and specifically the size of cells or dendrites—plays an important role on strength in materials produced by fusion-based AM processes [48,50]. The strengthening effect is thought to arise from dislocation pile ups and solute-enriched chemical boundaries found at cells/dendrites boundaries, which hinder plasticity. In general, the dislocation density at these sub-grain structures can be estimated from the cell or dendrite spacing and the corresponding strengthening contribution can be computed using the Bailey-Hirsh relation [49]. In our sample H, the relatively large dendrite size (> 10 μm) is probably the reason why the contribution from σ_{PDAS} to the hardness variation is not a major one. By contrast, we find the strengthening mechanisms linked to Nb concentration in the γ matrix to be the dominant ones, contributing to 68% of the overall hardness variation. Nb acts to strengthen the Ni-base alloy either when in solid solution [47], or when it forms secondary-phases—namely the γ'' and δ precipitates—after heat treatment. The high σ_{SS} value is intuitive when considering that Nb has close to the largest lattice mismatch with Ni of any element that disperses into a substitutional solid solution (+18%). In addition, $\sigma_{\gamma''}$ is widely reported as the main strengthening mechanism at play in I718. As the CR decreases, we measure a reduction in the Nb concentration within dendrites (by EDS) and, in turn, we speculate a lower volume fraction of γ''. Therefore, we ascribe the progressively lower hardness along Z to the combined decrease in σ_{SS} and $\sigma_{\gamma''}$; which are directly linked to the variations in

Nb concentration arising from the change in CR along Z. We also believe that the progressive increase in δ precipitates along Z has negligible effects on the sample hardness, as previously reported by other researchers [36,37].

4.2. Heterogeneity along the transversal direction

Besides these complex microstructure changes along Z, we measure substantial differences in texture and grain size along the transversal direction too (corresponding to the X-axis in Fig. 5a). These changes are best appreciated in the R sample owing to its larger size. We believe that this transversal microstructure gradients stem from a variable thermal buildup along the X axis, which results from the off-centered position of the build onto the substrate. Indeed, as shown in Fig. 5a, material deposition started at 12 mm and 34 mm from the substrate corner along X and Y, respectively. Since the thermal mass of the substrate is asymmetrically distributed around this build, it may induce an equally asymmetric thermal flux—and thus CR—along the transversal direction. As a result, we find larger, columnar grains with stronger < 100 > texture at left-hand side of the R sample (from where we took the compression samples color-coded in purple in Fig. 5a) compared to the right-hand side column (color-coded in blue in Fig. 5a).

To investigate the effects of these transversal gradients (both in texture and grain size) on the mechanical behavior of the build, we correlate the grain size with yield strength and estimate the Hall-Petch hardening effect expected from the grain size reduction, shown in Fig. 11. Interestingly, we observe that a linear Hall-Petch relationship cannot fit all data points at once. Instead, we need use three separate linear fits on the three sets of data points coming from the left, central, and right column of compression cylinders taken from the R sample. Noteworthy is that the Hall-Petch slope decreases from the left-hand side to the right-hand side of the sample. We attribute this result to texture variations along the transversal direction, which have shown to affect the relationship between yield strength and grain size. Godon et al. [45] for instance, showed that a randomly textured microstructures yield lower Hall–Petch slope compared to textured ones due the fundamentally different deformation mechanisms at play at grain boundaries. Random textures comprise larger number fraction of high-angle grain boundaries, which promote the formation of larger dislocation pile-ups and strain gradients. By contrast, they attributed a higher Hall–Petch slope in textured microstructures to a lower density of dislocation sources—because of the lower fraction of high-angle grain boundaries—as well as to limited grain boundary shearing of the copious low-angle grain boundaries. Another possible interpretation of the mechanical anisotropy found along X is the presence of microstructure "bands" in sample R (similarly to those found in sample H), which are more prominent on the right-hand side of the build (Fig. 2a). Kong et al. [52] suggested that localized microstructure heterogeneities such as these "bands" may induce stress buildups in AM component. This additional strengthening mechanism—which is less prominent within the strongly texture and more uniform microstructure found at the left-hand side of the sample—could also contribute to lowering the Hall-Petch slope along the X-axis. We are investigating the localized deformation of these microstructure more in detail and plan to present the results in a follow up study.

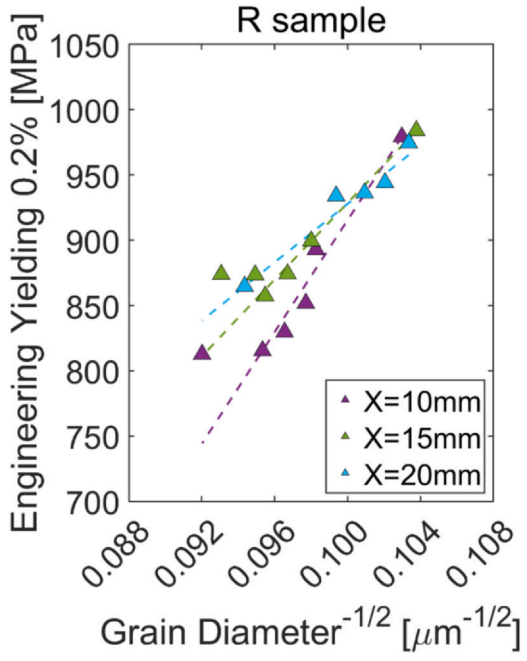

Fig. 11. Hall-Petch law. Hall-Petch law computed by correlation of the yielding data and average grain diameter on R sample.

4.3. Concluding remarks

Taken holistically, our results showcase the non-obvious relationships between the complex, multiscale microstructure heterogeneity of parts produced by DED processes and materials mechanical properties. In our study, the grain structure and texture heterogeneity in I718 samples produced using high energy input (i.e., the H and R samples) play a major role on the yield strength and Young's modulus anisotropy which we measure throughout the build. In theory, this heterogeneity could be mitigated through specially designed heat-treatments. However, those suggested by AMS standards (which we employed in this study) are not amenable to homogenize the microstructure. Another possible approach to mitigate this problem may lie in careful selection of DED process parameters to reduce segregation of elements in inter-dendritic regions. The thermal stability of alloys produced by means of fusion-based AM processes is known to be function of the solidification structure and, more specifically, of the amount of solute that segregates at the solid/liquid interface during rapid solidification [9]. This solidification structure can be controlled, indirectly, by tuning the laser parameters, which affect the solidification velocity within the melt pool. An alloy that recrystallizes at the temperatures required for solution hardening would exhibit a uniform microstructure and uniform mechanical properties; regardless of the complexity and heterogeneity found in the as-built material. The drawback in such an approach is that the mechanical properties of recrystallized microstructures are, generally, worse than those found in rapidly solidified alloys [9].

Our study also highlights the permanent impact that the segregation of solute—in this case Nb—leaves on hardness. Due to the slow diffusion of Nb through Ni and the relatively large dendrite spacing (on the order of 10 μm), the required heat treatment time for Nb homogenization would be prohibitive. Faster cooling rate results in less Nb concentration in inter-dendritic regions and more consistent mechanical behavior, as demonstrated by our results on the L sample. However, the more homogeneous microstructure and mechanical properties of the L sample come at the cost of a greatly reduced build rate, which may adversely affect the economic advantages offered by DED. Maintaining a consistent CR throughout a build without compromising throughput is thus of paramount importance in DED processes. One possible approach to achieve a uniform CR could be to use preheated substrates [34]. However, there are chances that this approach may overall decrease the mechanical properties of the alloy due to the lower CR.

This work demonstrates property variability within cuboid samples. It is reasonable to assume that these effects would be further amplified by a more complex part geometry, wherein the multidirectional thermal gradients could yield even more dramatic microstructure heterogeneity. When it is impossible or inefficient to modify the building strategy to accommodate sample heating, it is important to understand the effect that a variable CR will have on the part. Elemental segregation like that observed here can have a variety of detrimental effects. Superalloys like I718 are particularly susceptible to this problem due to the variety of elements present. However, even in stainless steels the segregation of chromium into cellular solidification structures can compromise the corrosion resistance of a part or lead to mechanical inhomogeneity [39,40].

More generally, AM is an emerging field with widespread promise for geometrically customized manufacturing. However, due to the unique thermal environment during metal AM—and DED in particular—the local thermal history of a part can be inconsistent, leading to a multiscale microstructure heterogeneity that has non-obvious implications on the mechanical properties on the resulting build. Counteracting these shortcomings may be possible by devising more adaptive build strategies that consider both the physical properties of the material being deposited as well as the geometric properties of the desired part. A combination of insightful build strategies and realistic engineering controls on AM parts is necessary to maximize the application of additive technologies while mitigating risks that could be associated with local property variation.

5. Main conclusion

The main conclusion of this work are:

- The high thermal input associated with high build rate DED processes may yield a multiscale structural heterogeneity, which includes large-scale microstructure “bands” of equiaxed grains with possibly dissimilar crystallographic textures with respect to the prevailing columnar growth, as well as local gradients in both composition and second phase precipitate structures. Such a heterogeneity cannot be removed using standard heat treatments.
- We ascribe the microstructure “bands” to layer-wise differences in cooling rate, which can be directly related to the deposition strategy we employed. Conversely, composition gradients and precipitate structure variations stem from a progressively lower cooling rate as the build progresses, which results from the increasingly longer distance of the melt pool to the heat sink (i.e., the base plate).
- We assess the property scatter induced by this multiscale microstructure heterogeneity using a combination of indentation and compression tests. We find that hardness variations correlate well with changes in Nb content in γ matrix and size of the dendrites. By contrast, bulk mechanical properties are strongly affected by changes in texture (from < 100 > to random) and grain size. Interestingly, the correlation between the average grain diameter and the mechanical properties does not generate a linear Hall-Petch relationship, whose slope appears to be affected by the local crystallographic texture.
- Homogeneous microstructure and consistent mechanical properties may be attained by proper control of the cooling rate and specially designed deposition strategies during DED. Through careful selection of the process parameter, it is possible to manipulate the thermal build up and thus the cooling rate to achieve the desired microstructure. In some cases, however, such achievements may come at the cost of a significantly reduced build rate.

CRediT authorship contribution statement

Yeoh Yong Chen: Methodology, Formal analysis, Investigation, Writing – review & editing. **Guido Macchi**: Conceptualization, Methodology, Software, Writing – review & editing. **Ekta Jain**: Investigation, Resources. **Bernard Gaskey**: Conceptualization, Writing – original draft. **Sudharshan Raman**: Validation. **Grace Tay**: Resources, Validation. **Davide Verdi**: Resources, Validation. **Alin Patran**: Supervision. **Antonio Mattia Grande**: Supervision. **Matteo Seita**: Supervision, Project administration, Funding acquisition.

Data availability

The raw data (machine parameter) required to reproduce these findings cannot be shared at this time due to industry proprietary issues. The characterization data are available upon request.

Declaration of Competing Interest

The authors declare that they have no known competing financial interests or personal relationships that could have appeared to influence the work reported in this paper.

Acknowledgments

This research was funded by the National Research Foundation (NRF) Singapore, under the NRF Fellowship program (NRF-NRFF2018–05), and by STE Aerospace Pte. Ltd. YYC and EJ are supported by Nanyang Technological University Singapore (NTU) and the Ministry of Education of Singapore through an Industrial Postgraduate Programme (IPP) scholarship (M4062246) and the collaboration with the University of Strathclyde, UK, respectively. The authors would like to acknowledge the Singapore Centre for 3D printing for providing the 3D printing facility, NTU for providing access to materials characterization facilities, and ARTC for the support with the deposition work.

Appendix A. Supporting information

Supplementary data associated with this article can be found in the online version at doi:10.1016/j.jallcom.2021.161426.

References

[1] S. Thompson, L. Bian, N. Shamsaei, A. Yadollahi, An overview of direct laser deposition for additive manufacturing; part I: transport phenomena, modeling and diagnostics, Addit. Manuf. 8 (2015) 36–62, https://doi.org/10.1016/j.addma.2015.07.001
[2] A. Dass, A. Moridi, State of the art in directed energy deposition: From additive manufacturing to materials design, Coatings 9 (2019) 1–26, https://doi.org/10.3390/COATINGS9070418
[3] S. Kaierle, L. Overmeyer, I. Alfred, B. Rottwinkel, J. Hermsdorf, V. Wesling, N. Weidlich, Single-crystal turbine blade tip repair by laser cladding and remelting, CIRP J. Manuf. Sci. Technol. 19 (2017) 196–199, https://doi.org/10.1016/j.cirpj.2017.04.001
[4] R.R. Ma, J.T. Belter, A.M. Dollar, Hybrid deposition manufacturing: design strategies for multimaterial mechanisms via three- dimensional printing and material deposition, J. Mech. Robot. 7 (2015) 1–10, https://doi.org/10.1115/1.4029400
[5] X. Zhao, J. Chen, X. Lin, W. Huang, Study on microstructure and mechanical properties of laser rapid forming Inconel 718, Mater. Sci. Eng. A. 478 (2008) 119–124, https://doi.org/10.1016/j.msea.2007.05.079
[6] A.S. Johnson, S. Shao, N. Shamsaei, S.M. Thompson, L. Bian, Microstructure, fatigue behavior, and failure mechanisms of direct laser-deposited Inconel 718, Jom 69 (2017) 597–603, https://doi.org/10.1007/s11837-016-2225-2
[7] B. Chen, J. Mazumder, Role of process parameters during additive manufacturing by direct metal deposition of Inconel 718, Rapid Prototyp. J. 23 (2017) 919–929, https://doi.org/10.1108/RPJ-05-2016-0071
[8] P.L. Blackwell, The mechanical and microstructural characteristics of laser-deposited IN718, J. Mater. Process. Technol. 170 (2005) 240–246, https://doi.org/10.1016/j.jmatprotec.2005.05.005

[9] S. Gao, Z. Hu, M. Duchamp, P.S.S.R. Krishnan, S. Tekumalla, X. Song, M. Seita, Recrystallization-based grain boundary engineering of 316L stainless steel produced via selective laser melting, Acta Mater. 200 (2020) 366–377, https://doi.org/10.1016/j.actamat.2020.09.015

[10] L.N. Carter, C. Martin, P.J. Withers, M.M. Attallah, The influence of the laser scan strategy on grain structure and cracking behaviour in SLM powder-bed fabricated nickel superalloy, J. Alloy. Compd. 615 (2014) 338–347, https://doi.org/10.1016/j.jallcom.2014.06.172

[11] V.A. Popovich, E.V. Borisov, A.A. Popovich, V.S. Sufiiarov, D.V. Masaylo, L. Alzina, Functionally graded Inconel 718 processed by additive manufacturing: crystallographic texture, anisotropy of microstructure and mechanical properties, Mater. Des. 114 (2017) 441–449, https://doi.org/10.1016/j.matdes.2016.10.075.L

[12] M.L. Thijs, R. Montero Sistiaga, Q. Wauthle, J.P. Xie, J. Van Humbeeck Kruth, Strong morphological and crystallographic texture and resulting yield strength anisotropy in selective laser melted tantalum, Acta Mater. 61 (2013) 4657–4668, https://doi.org/10.1016/j.actamat.2013.04.036

[13] B. Ferrar, L. Mullen, E. Jones, R. Stamp, C.J. Sutcliffe, Gas flow effects on selective laser melting (SLM) manufacturing performance, J. Mater. Process. Technol. 212 (2012) 355–364, https://doi.org/10.1016/j.jmatprotec.2011.09.020

[14] G.E. Bean, T.D. McLouth, D.B. Witkin, S.D. Sitzman, P.M. Adams, R.J. Zaldivar, Build orientation effects on texture and mechanical properties of selective laser melting Inconel 718, J. Mater. Eng. Perform. 28 (2019) 1942–1949, https://doi.org/10.1007/s11665-019-03980-w

[15] R. Cunningham, C. Zhao, N. Parab, C. Kantzos, J. Pauza, K. Fezzaa, T. Sun, A.D. Rollett, Keyhole threshold and morphology in laser melting revealed by ultrahigh-speed x-ray imaging, Science 363 (2019) 849–852, https://doi.org/10.1126/science.aav4687

[16] F. Lia, J.Z. Park, J. Keist, S. Joshi, R. Martukanitz, Thermal and microstructural analysis of laser-based directed energy deposition for Ti-6Al-4V and Inconel 625 deposits, Mater. Sci. Eng. A 717 (2018) 1–10, https://doi.org/10.1016/j.msea.2018.01.060

[17] Z. Li, J. Chen, S. Sui, C. Zhong, X. Lu, X. Lin, The microstructure evolution and tensile properties of Inconel 718 fabricated by high-deposition-rate laser directed energy deposition, Addit. Manuf. 31 (2020) 100941, https://doi.org/10.1016/j.addma.2019.100941

[18] S. Sui, H. Tan, J. Chen, C. Zhong, Z. Li, W. Fan, A. Gasser, W. Huang, The influence of Laves phases on the room temperature tensile properties of Inconel 718 fabricated by powder feeding laser additive manufacturing, Acta Mater. 164 (2019) 413–427, https://doi.org/10.1016/j.actamat.2018.10.032

[19] B.C. Salzbrenner, J.M. Rodelas, J.D. Madison, B.H. Jared, L.P. Swiler, Y.L. Shen, B.L. Boyce, High-throughput stochastic tensile performance of additively manufactured stainless steel, J. Mater. Process. Technol. 241 (2017) 1–12, https://doi.org/10.1016/j.jmatprotec.2016.10.023

[20] S. Huang, S.L. Sing, G. de Looze, R. Wilson, W.Y. Yeong, Laser powder bed fusion of titanium-tantalum alloys: compositions and designs for biomedical applications, J. Mech. Behav. Biomed. Mater. 108 (2020) 103775, https://doi.org/10.1016/j.jmbbm.2020.103775

[21] A. Arabi-Hashemi, X. Maeder, R. Figi, C. Schreiner, S. Griffiths, C. Leinenbach, 3D magnetic patterning in additive manufacturing via site-specific in-situ alloy modification, Appl. Mater. Today 18 (2020) 100512, https://doi.org/10.1016/j.apmt.2019.100512

[22] E. Hosseini, V.A. Popovich, A review of mechanical properties of additively manufactured Inconel 718, Addit. Manuf. 30 (2019) 100877, https://doi.org/10.1016/j.addma.2019.100877

[23] Nickel Alloy, Corrosion and Heat Resistant, Bars, Forgings, and Rings 52.5Ni 19Cr 3.0Mo 5.1Cb 0.90Ti 0.50Al 19Fe, AMS,, 1965, p. 5663.

[24] ASTM, Standard Practice for Microetching Metals and Alloys, ASTM Int. West Conshohocken, 2007, https://doi.org/10.1520/E0407-07E01

[25] Agilent, Agilent Nano Indenter G200 User Manual, 2013: 1–4.

[26] H. Wang, A. Dhiman, H.E. Ostergaard, Y. Zhang, T. Siegmund, J.J. Kruzic, V. Tomar, Nanoindentation based properties of Inconel 718 at elevated temperatures: a comparison of conventional versus additively manufactured samples, Int. J. Plast. 120 (2019) 380–394, https://doi.org/10.1016/j.ijplas.2019.04.018

[27] M.E. Aydinöz, F. Brenne, M. Schaper, C. Schaak, W. Tillmann, J. Nellesen, T. Niendorf, On the microstructural and mechanical properties of post-treated additively manufactured Inconel 718 superalloy under quasi-static and cyclic loading, Mater. Sci. Eng. A. 669 (2016) 246–258, https://doi.org/10.1016/j.msea.2016.05.089

[28] S. Katayama, A. Matsunawa, Solidification microstructure of laser welded stainless steels, LIA (Laser Inst. Am. 60 (1984) 1–8, https://doi.org/10.2351/1.5057623

[29] W. Kurz, D.J. Fisher, Fundamentals of solidifications, 1998.

[30] D.M. Stefanescu, Science and engineering of casting solidification: Third edition, 2015. ⟨https://doi.org/10.1007/978–3-319–15693-4⟩.

[31] W. Zhang, L. Liu, X. Zhao, T. Huang, Z. Yu, M. Qu, H. Fu, Effect of cooling rates on dendrite spacings of directionally solidified DZ125 alloy under high thermal gradient, Rare Met. 28 (2009) 633–638, https://doi.org/10.1007/s12598-009-0121-4

[32] M.H. Farshidianfar, A. Khajepour, A.P. Gerlich, Effect of real-time cooling rate on microstructure in Laser Additive Manufacturing, J. Mater. Process. Technol. 231 (2016) 468–478, https://doi.org/10.1016/j.jmatprotec.2016.01.017

[33] L.L. Parimi, G. Ravi, D. Clark, M.M. Attallah, Microstructural and texture development in direct laser fabricated IN718, Mater. Charact. 89 (2014) 102–111, https://doi.org/10.1016/j.matchar.2013.12.012

[34] N.A. Kistler, A.R. Nassar, E.W. Reutzel, D.J. Corbin, A.M. Beese, Effect of directed energy deposition processing parameters on laser deposited Inconel ® 718: Microstructure, fusion zone morphology, and hardness, J. Laser Appl. 29 (2017) 022005, https://doi.org/10.2351/1.4979702

[35] M. Ma, Z. Wang, X. Zeng, Effect of energy input on microstructural evolution of direct laser fabricated IN718 alloy, Mater. Charact. 106 (2015) 420–427, https://doi.org/10.1016/j.matchar.2015.06.027

[36] M. Anderson, A.L. Thielin, F. Bridier, P. Bocher, J. Savoie, δ Phase precipitation in Inconel 718 and associated mechanical properties, Mater. Sci. Eng. A. 679 (2017) 48–55, https://doi.org/10.1016/j.msea.2016.09.114

[37] M. Burke, M.K. Miller, Precipitation in Alloy 718: A combined AEM and APFIM investigation, in: Superalloys, 1991: pp. 337–350. https://doi.org/10.7449/1991/Superalloys_1991_337_350.

[38] Z.C. Cordero, B.E. Knight, C.A. Schuh, Six decades of the Hall–Petch effect – a survey of grain-size strengthening studies on pure metals, Int. Mater. Rev. 61 (2016) 495–512, https://doi.org/10.1080/09506608.2016.1191808

[39] Y.M. Wang, T. Voisin, J.T. McKeown, J. Ye, N.P. Calta, Z. Li, Z. Zeng, Y. Zhang, W. Chen, T.T. Roehling, R.T. Ott, M.K. Santala, P.J. Depond, M.J. Matthews, A.V. Hamza, T. Zhu, Additively manufactured hierarchical stainless steels with high strength and ductility, Nat. Mater. 17 (2018) 63–70, https://doi.org/10.1038/NMAT5021

[40] A. Leicht, M. Rashidi, U. Klement, E. Hryha, Effect of process parameters on the microstructure, tensile strength and productivity of 316L parts produced by laser powder bed fusion, Mater. Charact. 159 (2020) 110016, https://doi.org/10.1016/j.matchar.2019.110016

[41] H.L. Wei, J. Mazumder, T. DebRoy, Evolution of solidification texture during additive manufacturing, Sci. Rep. 5 (2015) 1–7, https://doi.org/10.1038/srep16446

[42] V.A. Popovich, E.V. Borisov, A.A. Popovich, V.S. Sufiiarov, D.V. Masaylo, L. Alzina, Functionally graded Inconel 718 processed by additive manufacturing: crystallographic texture, anisotropy of microstructure and mechanical properties, Mater. Des. 114 (2017) 441–449, https://doi.org/10.1016/j.matdes.2016.10.075

[43] S.Y. Liu, H.Q. Li, C.X. Qin, R. Zong, X.Y. Fang, Mechanical vibration-extracted stromal vascular fraction improves volume retention after autologous fat grafting, Plast. Reconstr. Surg. 146 (2020) 1275–1284, https://doi.org/10.1016/j.matdes.2020.108642

[44] M. Kamaya, A procedure for estimating Young's modulus of textured polycrystalline materials, Int. J. Solids Struct. 46 (13) (2009) 2642–2649, https://doi.org/10.1016/j.ijsolstr.2009.02.013

[45] O. Gokcekaya, T. Ishimoto, S. Hibino, J. Yasutomi, T. Narushima, T. Nakano, Unique crystallographic texture formation in Inconel 718 by laser powder bed fusion and its effect on mechanical anisotropy, Acta Mater. 212 (2021) 116876.

[46] K.A. Sofinowski, S. Raman, X. Wang, B. Gaskey, M. Seita, Layer-wise engineering of grain orientation (LEGO) in laser powder bed fusion of stainless steel 316L, Addit. Manuf. 38 (2021) 101809.

[47] D. Kong, C. Dong, X. Ni, L. Zhang, C. Man, J. Yao, Y. Ji, Y. Ying, K. Xiao, X. Cheng, X. Li, High-throughput fabrication of nickel-based alloys with different Nb contents via a dual-feed additive manufacturing system: effect of Nb content on microstructural and mechanical properties, J. Alloy. Compd. 785 (2019) 826–837, https://doi.org/10.1016/j.jallcom.2019.01.263

[48] D. Kong, C. Dong, S. Wei, X. Ni, L. Zhang, R. Li, L. Wang, C. Man, X. Li, About metastable cellular structure in additively manufactured austenitic stainless steels, Addit. Manuf. 38 (December 2020) (2021), https://doi.org/10.1016/j.addma.2020.101804

[49] S. Zhang, X. Lin, L. Wang, X. Yu, Y. Hu, H. Yang, L. Lei, W. Huang, Strengthening mechanisms in selective laser-melted Inconel718 superalloy, Mater. Sci. Eng. A 812 (March) (2021), https://doi.org/10.1016/j.msea.2021.141145

[50] K. Ma, H. Wen, T. Hu, T.D. Topping, D. Isheim, D.N. Seidman, E.J. Lavernia, J.M. Schoenung, Mechanical behavior and strengthening mechanisms in ultrafine grain precipitation-strengthened aluminum alloy, Acta Mater. 62 (1) (2014) 141–155, https://doi.org/10.1016/j.actamat.2013.09.042

[51] W.J. Oh, W.J. Lee, M.S. Kim, J.B. Jeon, D.S. Shim, Repairing additive-manufactured 316L stainless steel using direct energy deposition, Opt. Laser Technol. 117 (February) (2019) 6–17, https://doi.org/10.1016/j.optlastec.2019.04.012

[52] D. Kong, C. Dong, X. Ni, Z. Liang, C. Man, X. Li, Hetero-deformation-induced stress in additively manufactured 316L stainless steel, Mater. Res. Lett. 8 (10) (2020) 390–397, https://doi.org/10.1080/21663831.2020.1775149